Since January 2020 Elsevier has created a COVID-19 resource centre with free information in English and Mandarin on the novel coronavirus COVID-19. The COVID-19 resource centre is hosted on Elsevier Connect, the company's public news and information website.

Science of the Total Environment 750 (2021) 142323

Contents lists available at ScienceDirect

Science of the Total Environment

journal homepage: www.elsevier.com/locate/scitotenv

Impact of emission reductions and meteorology changes on atmospheric mercury concentrations during the COVID-19 lockdown

Qingru Wu [a,b], Yi Tang [a], Long Wang [c], Shuxiao Wang [a,b,*], Deming Han [a], Daiwei Ouyang [a], Yueqi Jiang [a], Peng Xu [d], Zhigang Xue [d], Jingnan Hu [d]

[a] State Key Joint Laboratory of Environmental Simulation and Pollution Control, School of Environment, Tsinghua University, Beijing 100084, China
[b] State Environmental Protection Key Laboratory of Sources and Control of Air Pollution Complex, Beijing 100084, China
[c] Guangdong Provincial Academy of Environmental Science, Guangdong Provincial Environmental Protection Key Laboratory of Atmospheric Environment Management and Policy Simulation, Guangzhou 510045, China
[d] Chinese Research Academy of Environmental Sciences, Beijing 100012, China

HIGHLIGHTS

- The effect of lock-down measures on atmospheric Hg was quantified by generalized additive model.
- Atmospheric mercury responded almost linearly to the changes in mercury emissions when excluding the impact of other factors.
- Meteorology with enhanced relative humidity and temperature reduced emission reduction' effect during the lockdown sub-period

GRAPHICAL ABSTRACT

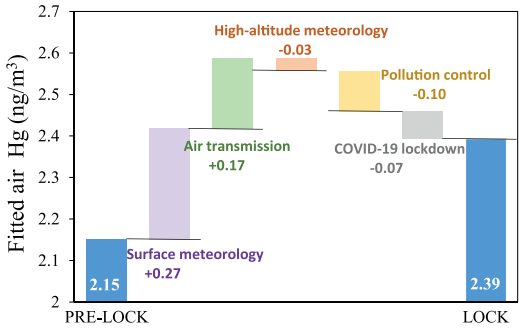

ARTICLE INFO

Article history:
Received 6 August 2020
Received in revised form 8 September 2020
Accepted 8 September 2020
Available online 11 September 2020

Editor: Jianmin Chen

Keywords:
Atmospheric mercury
Emission reduction
Meteorology change
COVID-19

ABSTRACT

Controlling anthropogenic mercury emissions is an ongoing effort and the effect of atmospheric mercury mitigation is expected to be impacted by accelerating climate change. The lockdown measures to restrict the spread of Coronavirus Disease 2019 (COVID-19) and the following unfavorable meteorology in Beijing provided a natural experiment to examine how air mercury responds to strict control measures when the climate becomes humid and warm. Based on a high-time resolution emission inventory and generalized additive model, we found that air mercury concentration responded almost linearly to the changes in mercury emissions when excluding the impact of other factors. Existing pollution control and additional lockdown measures reduced mercury emissions by 16.7 and 12.5 kg/d during lockdown, respectively, which correspondingly reduced the concentrations of atmospheric mercury by 0.10 and 0.07 ng/m^3. Emission reductions from cement clinker production contributed to the largest decrease in atmospheric mercury, implying potential mitigation effects in this sector since it is currently the number one emitter in China. However, changes in meteorology raised atmospheric mercury by 0.41 ng/m^3. The increases in relative humidity (9.5%) and temperature (1.2 °C) significantly offset the effect of emission reduction by 0.17 and 0.09 ng/m^3, respectively, which highlights the challenge of air mercury control in humid and warm weather and the significance of understanding mercury behavior in the atmosphere and at atmospheric interfaces, especially the impact from relative humidity.

* Corresponding author at: State Environmental Protection Key Laboratory of Sources and Control of Air Pollution Complex, Beijing 100084, China.
E-mail address: shxwang@tsinghua.edu.cn (S. Wang).

https://doi.org/10.1016/j.scitotenv.2020.142323
0048-9697/

1. Introduction

Mercury (Hg) pollution has caused global concern due to its long-range transmission, bio-toxicity, and neurotoxicity (Chen et al., 2019; Gianga and Selina, 2016; Horowitz et al., 2017; Liu et al., 2019a). To protect human beings and the environment from Hg emissions and releases, the *Minamata Convention on Mercury* (abbreviated as Convention) was signed in 2013 and has been taken into force since 2017 (UNEP, 2013). Parties are required to reduce anthropogenic emissions and evaluate the effectiveness of emission control.

Almost simultaneously, China took aggressive air pollution control measures during 2013–2017 to mitigate domestic haze pollution by launching the *Air Pollution and Prevention Action Plan* (SC, 2013). A series of measures have been adopted, such as the ultra-low emission retrofit in coal-fired power plants (CFPP), eliminating backward production capacity, enhancing traditional air pollution control measures in industrial sources, replacing residential coal with electricity and natural gas, and off-peak production in winter. These strict policies effectively led to the reduction of atmospheric Hg emissions as a co-benefit (Liu et al., 2018; Tian et al., 2015; Wen et al., 2020; Wu et al., 2018a, 2017, 2018b). Atmospheric Hg emissions were reduced by approximately 22% from 2013 to 2017 (Liu et al., 2019b). Correspondingly, the decrease of annual atmospheric Hg concentrations (TM) were observed at both urban sites and rural sites during 2013–2017 (Tang et al., 2018; Yin et al., 2018).

Afterwards, China released the *Three-year Action Plan for Clean Air* to further the effectiveness of air pollution control (SC, 2018). In addition, to control the spread of the 2019 Novel Coronavirus (COVID-19), China issued a series of lockdown measures such as conditional industrial resumption, which indirectly led to restrictions in certain industrial activities. Such an emission scenario with strict pollution control and weakened industry demand is expected to occur in the coming ten years when China enters the post-industrial era (Wu et al., 2018a). Therefore, we are interested to learn to what extent atmospheric Hg emissions can be reduced under the joint measures of existing pollution control and the additional COVID-19 lockdown during this special period. Coincidentally, meteorology data has indicated that the relative humidity in East China during the lockdown period was the highest across the past ten years, and the average temperature increased by approximately 1.6 °C compared to the same period in 2019. The appearance of this kind of humid and warm weather is a silhouette of future climate change (IPCC, 2014). Thus, the tragic outbreak of COVID-19 provides a natural experiment to find how atmospheric Hg (TM) responds to anthropogenic Hg emission reductions when the climate becomes humid and warm.

In this study, we firstly compiled an Hg emission inventory with an hourly resolution to find the emission reductions due to anthropogenic control measures. Then, we established the relationship between TM concentrations and emissions, as well as meteorological fields, by applying a generalized additive model. Finally, by using the scenario analysis method, we predicted the response of TM to the change in anthropogenic measures and various meteorological parameters. By conducting this study, we aim to elucidate how policy and science can be prepared to better control TM pollution and implement the Convention.

2. Methodology

2.1. Anthropogenic emissions

We applied our China Atmospheric Mercury Emission (CAME) model to compile the anthropogenic emission inventory (Hui et al., 2017; Liu et al., 2018, 2019b; Wu et al., 2016, 2018b; Zhang et al., 2015). This model covers almost all emission sectors (29 sectors) in the *Mercury Assessment Report*. The inventory contains monthly emissions and approximately 13 types of sources are point sources (covering more than 70% of emissions in 2017). This model estimates Hg emissions based on the mass-balance method and considers Hg input and removal in the studied sectors. The database for this model included Hg content of raw materials/fuel, coal quality, activity level, types of air pollution control device (APCD) combinations, and Hg removal and speciation for different types of APCDs.

In this study, we applied this model to compile the high-time resolution Hg emission inventory. We focused on the emissions in the Beijing-Tianjin-Hebei (BTH) region because this area is the main Hg emission region in China. It is also the source area of Hg emissions for our observation site based on the Potential Source Contribution Factors result (Tang et al., 2019). The studied period was from Jan 1, 2020 to Mar 10, 2020. China activated the First-Level Public Health Emergency Response in late January when strict lockdown measures were implemented, and economic activities gradually resumed after mid-February. Thus, we divided the studied period into three sub-periods based on the execution times of the COVID-19 lockdown measures. We denoted these three sub-periods as PRE_LOCK (Jan 1–Jan 19), LOCK (Jan 20–Feb 15), and AFTER_LOCK (Feb 16–Mar 10), respectively. Moreover, COVID-19 broke during the Chinese New Year and there were measures to control air pollutants. To separate the impact of existing measures and additional lockdown measures, we complied an additional emission inventory (em_BAU) for the studied period. We first compiled the 2019 emissions (em_2019) and derived the 2015–2017 emissions from the CAME model. Then, we assumed that the emission amount of each sector followed their emission trend from 2015 to 2019. This trend continued to 2020 and we obtained the em_BAU.

We followed most of the datasets in the CAME model, but we assumed that all new released capacity in 2019 and 2020 had applied advanced APCDs considering the strict pollution control requirement. We also updated the activity level based on a field and questionnaire investigation, literature review, and expert consultant. The detailed data sources are listed in Table S1. We obtained daily clinker yields for cement clinker production (CEM) by dividing the monthly production by the daily operation rate of production lines. We adopted a similar method for the iron and steel production sector (ISP). Daily coal consumption data of coal-fired power plants (CFPP) were from the Coal Electricity Group. Daily residential coal combustion (RCC) was based on the field and questionnaire investigation. We generated the coal consumption data for the heating supply sector (HS) based on the change of heating areas. Biomass combustion (BIO) was estimated based on the number of fire points. The change in coal consumption for the coking sector (COK) followed the change in crude steel production, considering that more than 80% of coke was produced in steel plants. Daily mobile oil combustion was adjusted based on oil combustion and the change in transportation data. For the other sectors, we simply calculated the emissions based on the change in activity level and then distributed them to a daily resolution. We finally improved the time resolution of the inventory to a 1-h resolution based on the hourly distribution coefficient (HDC) (Supporting information S1 and Fig. S1).

2.2. TM observations

We conducted TM observations in Tsinghua University, Haidian district of Beijing, China (Fig. S2). The sampling site (40.00 N, 116.33 E) was located at the top of the Environmental Engineering Laboratory Building. Only the campus and residential areas fell within a 1 km radius, and no industrial point sources were within a 30 km radius. It is a representative site for the atmospheric environment in urban Beijing, where many atmospheric observation experiments have been conducted over the years (Hu et al., 2020; Tang et al., 2019). We used atmospheric Hg monitoring system (Tekran™ 2537B/1130/1135)to monitor speciated Hg in the atmosphere, which has been widely used for atmospheric Hg observations around the world. Previous studies have described the principle of these instruments in detail, as well as routine maintenance for it (Supporting Information S2.3) (Fu et al., 2015; Landis et al., 2002; Sprovieri et al., 2016; Tang et al., 2018).

First, we obtained 5-min resolutions of gaseous elemental Hg (GEM) concentrations and 2-h resolutions of reactive gaseous Hg (RGM) and particulate-bound Hg (PBM) concentrations from the equipment. Then, we integrated the 5-min GEM concentrations to 1-h resolutions and interpolated the RGM and PBM concentrations to 1-h resolutions by averaging the two adjacent values. The summation of the three species was regarded as the total atmospheric Hg (TM) in this study. Considering that the proportion of active Hg (summation of RGM and PBM) accounted for less than 10% of total Hg during the studied and control period, the data disposal method had limited impact on the final TM concentrations. During the observation period, we encountered equipment failure from Feb 27–Mar 1, 2020. We used the multiple imputation method to impute the missing values of TM concentrations based on the highly linear correlation between CO and TM during the studied period (Fig. S3). CO concentration data were collected from the China National Environmental Monitoring Station (http://beijingair.sinaapp.com/).

2.3. Relationship between TM observations and impacting factors

We used a generalized additive model (GAM) to establish the relationship between TM and various variables, which have been used to simulate the changing trends of air pollutants (Gong et al., 2018, 2017). The GAM produces a simple and explicit formulation of response-predictor relationships in a neural network model (Aldrin and Haff, 2005). The equation is as follows:

$$g(\mu_i) = X_i\theta + f_1(x_{1i}) + f_2(x_{2i}) + \ldots + f_n(x_{ni}) + \xi_i \quad (1)$$

where i is the observation of the ith hour, g is the link function, and μ_i is the expectation of the dependent variable, which specifies the relationship between the linear formulation on the right side of Eq. (1) and the response μ_i. We used the "log" link function with a Gaussian distribution because the TM concentrations fitted a log-normal distribution. $X\theta$ is a constant component of the model, which presents a categorical relationship for predictors not subject to non-linear transformations. $f(x)$ is the smooth function of the predictors. The model building procedure can be divided into the following steps:

Step 1 dataset preparation

We prepared dataset_2020 for the studied period (Table S2). Based on the impact of the factors on TM variation, the dataset consisted of four subsets, including emission, surface meteorology, high-altitude meteorology, and air transmission. The background concentration in Beijing was assumed to be unchanged in such a short time. The impact of natural emissions can be represented, to some extent, by the surface meteorology over the studied period due to their significant collinearity (Qin et al., 2019). The emission subset contained the hourly sectoral Hg emissions. We used the summation of the sectoral emissions for model building. The surface meteorology data consisted of temperature, relative humidity, wind speed, wind direction, and atmospheric pressure, which were from the China Meteorological Data Service Center (http://data.cma.cn/). The high-altitude meteorology subset was composed of the boundary layer height, radiation, total cloud fraction, and air density. These data were derived from the Weather Research and Forecasting (WRF) model (Skamarock et al., 2008). We obtained the 24-h and 48-h backward trajectories from the Hybrid Single Particle Lagrangian Integrated Trajectory (HYSPLIT) Model to represent air transmission (Polissar et al., 1999).

Step 2 variable selection

According to Woods' study (Wood, 2013), it is best to use the p-values from the larger model rather than those calculated through model comparisons to assess whether or not a variable should be left in the model. Thus, we included all parameters of the dataset in the model and deleted the insignificant ones based on the significance (F-statistics) and p-value of each variable. We used Penalized Cubic Regression Splines for the smoothing function of each parameter to balance between not fitting the observed data well and overfitting the data by choosing an effective number of degrees of freedom. The restricted maximum likelihood approach was used to conduct the overall smoothness selection criteria. Finally, we obtained 9 independent parameters for the model (Table S2).

Step 3 model evaluation

The model evaluation results were shown in Tables S3, S4 and Fig. S4. We used the 10-fold cross validation method to evaluate the accuracy of the GAM models (Fushiki, 2009). The strong correlation, with a determination coefficient (R^2) of approximately 97%, demonstrated the accuracy of GAM (Table S3). The parameters in the GAM model explained 63.2% of the variance in TM concentrations and the adjusted R^2 reached 0.620 (Table S3). Thus, the independent variables could interpret the TM concentrations well. All the selected independent variables significantly correlated with TM concentrations (Table S4). The QQ-plot results showed that the GAM produced good results around the average concentration and had larger uncertainties in larger and lower values (Fig. S4a). The residuals vs predictors (Fig. S4b) and histogram of the residuals (Fig. S4c) showed an almost unbiased simulation of TGM. The sharp decrease in the autocorrelation of residuals reflected almost no lag days during the simulation (Fig. S4d). The model evaluation process validated the underlying assumptions of the homogeneity, normality, and independence of the GAM, and the results ensured the quality of the model.

2.4. Predicting the impact of emissions and meteorology during the LOCK of 2020

We used the scenario analysis method to predict the impact of emission reductions and meteorology changes on air Hg concentrations during the LOCK sub-period of 2020. The emissions and meteorology during the PRE_LOCK period were used for comparison. The fitted TM concentrations during the LOCK sub-period, which was predicted based on dataset_2020, was regarded as the BASE scenario. Then, we replaced the actual emissions during the LOCK sub-period with em_BAU (em_covid scenario), and the difference in TM between this scenario and the BASE was regarded as the impact of the COVID-19 lockdown. We normalized the emissions during the LOCK sub-period by using the hour-mean emissions from PRE-LOCK (em_ctrl scenario). The TM change between em_ctrl and BASE reflected the impact of existing pollution control measures. To set the other scenarios, the basic principle was that we normalized the studied parameter during the LOCK sub-period by using the hour-mean value from the PRE_LOCK sub-period and kept the others unchanged as the BASE scenario. Then, we ran the *predict.gam* command to generate TM concentrations. The difference in TM between the BASE and objected scenario represented the impact of the corresponding parameter.

3. Results and discussion

3.1. Anthropogenic Hg emissions during the studied period

Atmospheric Hg emissions in the BTH region were approximately 7.7 t during the studied period. Dominant sources presented various trends, especially CEM, RCC, CFPP, and ISP (Fig. 1a). CEM emitted the largest amount of Hg during PRE_LOCK, accounting for 28% of total Hg emissions, and then sharply reduced at the beginning of the LOCK sub-period. Such a decline almost returned to the PRE_LOCK level at the end of the LOCK sub-period. Contrary to the emissions from CEM, Hg emissions from RCC increased from 10.6 kg/d during the PRE_LOCK sub-period to 13.9 kg/d during the LOCK sub-period, increasing by approximately 31%. Then, the emissions gradually decreased to 6.1 kg/d in the AFTER_LOCK sub-period with the increase of temperature. As for CFPP, 1081 kg of Hg emissions were released during the studied

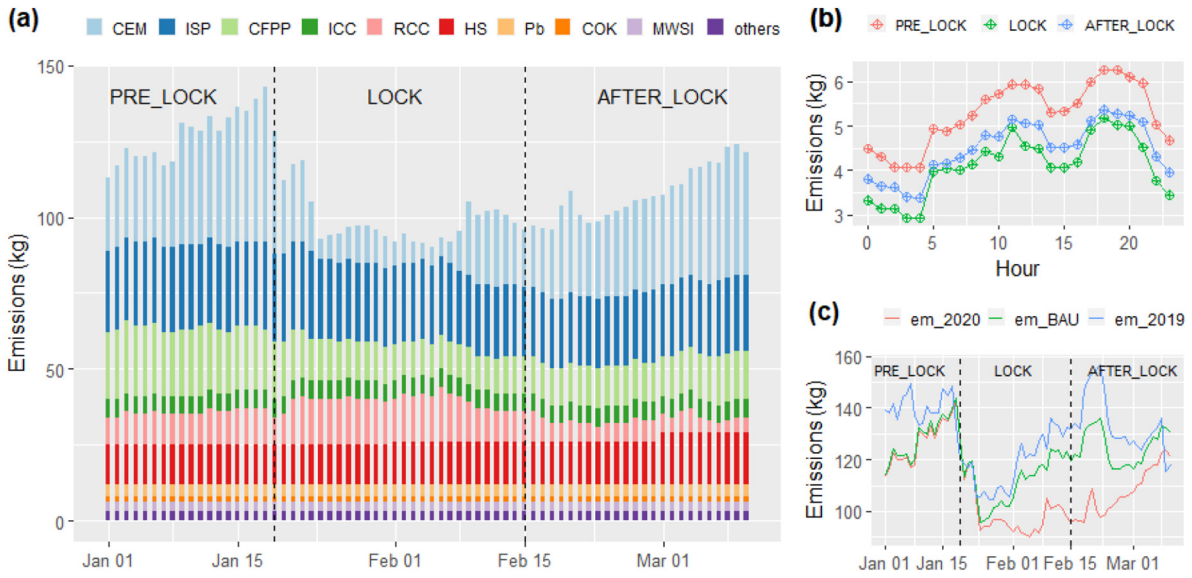

Fig. 1. Hg emissions. (a) Daily trend in the studied period; (b) hourly distribution in different sub-periods; (c) emission trend comparison (note: we used the timeline in 2020 as the x axis. The same period in 2019 was from Jan 12 to Mar 23.)

period. The daily mean value of Hg emissions during AFTER_LOCK was still 8.1 kg/d (37%) lower than that during PRE_LOCK. For ISP, daily Hg emissions during LOCK and AFTER_LOCK decreased by 7% and 13%, respectively. As for diurnal variation trends, they were almost the same, with two peaks around 11:00 and 18:00 and two troughs around 4:00 and 15:00, respectively (Fig. 1b). Compared with the sectoral HDC curve (Fig. S2), diurnal variations in the RCC and HS sectors drove such trends due to their relatively high emissions and violent fluctuations.

Under the combined impact of emissions from various sectors, Hg emissions in 2020 decreased from 128.4 ± 8.0 kg/d during PRE_LOCK to 99.2 ± 6.9 kg/d during LOCK, declining by approximately 22%. Then, Hg emissions increased to 106.6 ± 8.9 kg/d during the AFTER_LOCK sub-period. We observed an obvious emissions trough over the studied period in 2020. Such a trend was also observed in 2019 (Figs. 1c and S5); the trough in 2019 was due to the Chinese New Year. The lockdown measures extended the holiday and led to a wider trough in 2020. Additionally, the sharp increase in emissions after New Year in 2019 was replaced with a slower upward trend in 2020 due to the restriction of conditional work resumption. Thus, the daily mean Hg emissions during AFTER_LOCK were still 15% lower than those during PRE_LOCK, while daily mean values were almost the same during these two sub-periods in 2019.

Compared to the emissions in PRE-LOCK sub-period, the sharp decrease of Hg emission during the LOCK sub-period was the joint effect of existing pollution control measures due to Chinese New Year and the additional control effect of the COVID-19. Based on the emission trends from 2015 to 2019, we estimated the emissions in 2020 without the COVID-19 lockdown (em_BAU). Under this scenario, if we assumed that the emission control measures in the LOCK sub-period maintained the scenario in PRE-LOCK sub-period, then the emissions in the LOCK sub-period would have been 16.7 kg/d higher. That indicated the effect of existing control measures in the holiday of Chinese New Year. If we compared the em_BAU inventory and the actual emissions in 2020, the actual emissions during the LOCK sub-period were approximately 12.5 kg/d lower than the emissions in the same period of em_BAU scenario. This indicated the additional control effect of the COVID-19 lockdown measures. Therefore, anthropogenic emission control measures, including existing pollution control and the COVID-19 lockdown measures, jointly reduced Hg emissions by 29.2 kg/d during the LOCK sub-period.

3.2. Observed TM concentrations

TM concentrations were approximately 2.36 ± 0.90 ng/m^3 during the studied period. Compared with the Hg emission curve marked by an obvious trough during the LOCK sub-period, observed hourly TM concentrations fluctuated around a relative stable line with an insignificant decrease in 2020 (Fig. 2). When integrating the observed TM concentrations into three sub-periods, the mean TM concentration during the LOCK sub-period was approximately 15% higher than that in the other two periods. Thus, the observed TM concentrations almost contrasted with the emission trend and it seemed as if the observed TM concentrations did not directly correspond with the anthropogenic emissions from the LOCK sub-period of 2020.

However, when we compared the observed TM concentrations between the same period of 2019 and 2020, the mean TM concentrations in 2020 were 0.7 ng/m^3 lower than those in 2019. According to our recent study, the reduction of anthropogenic emissions drove the inter-annual decrease trend in Beijing from 2015 to 2018. The inter-annual decrease of both TM and anthropogenic emissions in 2019 and 2020 indicated that this trend continued into 2020. Anthropogenic Hg emissions are still a deciding factor for inter-annual TM reductions in Beijing currently. As for the TM concentrations in the control period of 2019, the mean values were 3.01 ± 1.61, 2.82 ± 0.91, and 3.31 ± 1.69 ng m^{-3} during the PRE_LOCK, LOCK, and AFTER_LOCK sub-periods, respectively. The TM concentrations also showed a similar trend to the emission trend in 2019. Therefore, the high Hg emission reduction but elevated TM increase during the LOCK sub-period indicated interferences from meteorology on emission control, which is described in the following section.

3.3. Drivers of TM variation during the LOCK sub-period

We built the GAM model for TM following the procedure in Section 2.3. The time series of both the observed and fitted TM concentrations generally showed good agreement (Fig. S6). The fitted TM concentrations were approximately 2.15 ± 0.53 ng/m^3 during the PRE_LOCK sub-period and 2.39 ± 0.63 ng/m^3 during the LOCK sub-period. Based on the scenario analysis, we predicted the contributions of different impacting factors. As shown in Fig. 3, anthropogenic control, including existing pollution control and the COVID-19 lockdown, drove TM reduction. During the LOCK sub-period, emission reduction due to

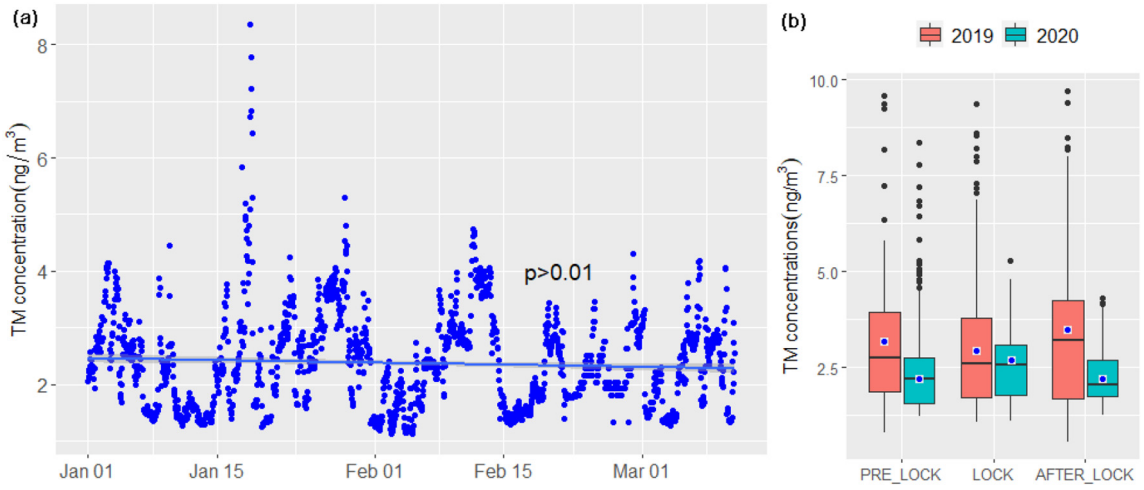

Fig. 2. Observed TM during the studied period and the comparison with that in 2019. (a) TM trend with time in 2020; (b) comparison of TM concentrations in different years.

existing pollution control and COVID-19 lockdown measures reduced TM concentrations by 0.10 and 0.07 ng/m^3, respectively. However, meteorology was overall unfavorable to the decrease of TM concentrations, increasing TM concentrations by 0.41 ng/m^3. Changes in surface meteorology and air transmissions raised TM concentrations by 0.27 and 0.17 ng/m^3, respectively, while high-altitude meteorology reduced TM concentrations by 0.03 ng/m^3. Therefore, the reduction of anthropogenic Hg emissions was almost offset by the changes in meteorology during the LOCK sub-period.

The influence of detailed parameters varied. TM concentrations increased almost linearly with the raise of anthropogenic emissions (Fig. 4a). Of all the sources, the emission reductions from CEM was the most significant and contributed to the decrease of TM concentrations by 0.11 ng/m^3 across the studied period (Table 1). Emission reductions from CEM were mainly caused by the effect of existing air pollution control measures, such as off-peak production. As for ISP and CFPP, TM concentrations were reduced by 0.01 ng/m^3 and 0.05 ng/m^3, respectively, due to emission reductions in these two sectors. Compared to these three sectors, the increased energy requirement from residential coal combustion increased TM concentrations by 0.02 ng/m^3 during the LOCK sub-period.

Surface meteorology increased TM concentrations by 0.27 ng/m^3 during the LOCK sub-period, mainly due to changes in relative humidity and temperature (Table 1). According to Fig. 4b, TM concentration increased with the raise of temperature, possibly because the increase of temperature would promote the Hg emissions from natural surface (Qin et al., 2019; Wang et al., 2016) (Horowitz et al., 2017). According to an empirical rule that a 10 °C temperature increase doubles the rates for chemical reactions near room temperature (Kissinger, 1957). This rule has been proved to be applicable to the reduction of oxidized Hg in boreal soil (Pannu et al., 2014). We observed a similar relationship between TM and relative humidity (Fig. 4c). The raise in relative humidity might enhance the liquid phase reduction process that converts reactive Hg to GEM (Horowitz et al., 2017; Huang et al., 2019; Saiz-Lopez et al., 2018). During the LOCK sub-period, hourly surface temperature and relative humidity increased by 1.2 °C and 9.5%, respectively, which correspondingly raised the TM by 0.09 and 0.17 ng/m^3. The increase in boundary layer height benefitted the reduction of TM concentrations by providing favorable diffusion conditions, as seen in Fig. S7a. Thus, the increased boundary height during the LOCK sub-period reduced overall TM concentrations by approximately 0.02 ng/m^3. The TM concentrations remained at a high level when the latitude of the 48-h trajectory was lower than 40°N (Fig. S7b). Thereafter, TM concentrations decreased with the increase in the latitude of the 48-h trajectory. This indicated that trajectories from the south of the monitoring sites embodied higher loads of Hg. Thus, when the proportion of

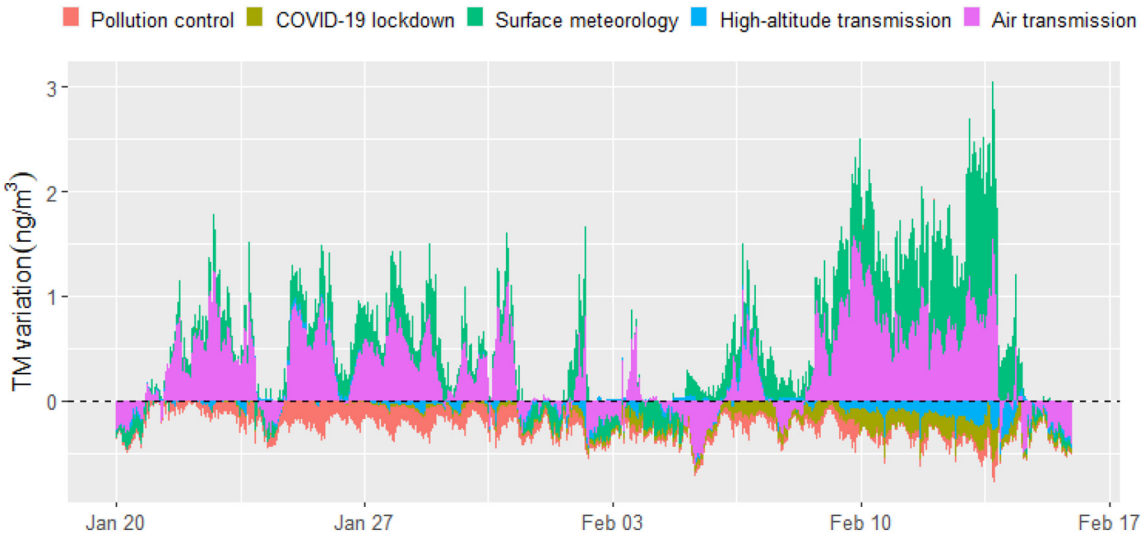

Fig. 3. The impact of variables on TM variation during LOCK sub-period.

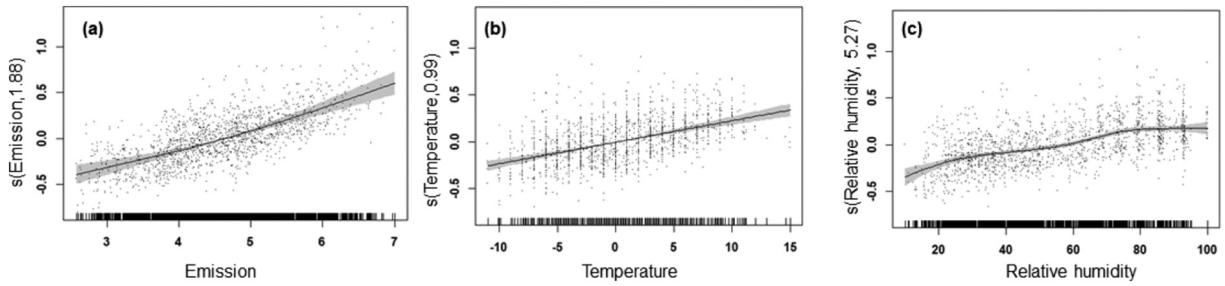

Fig. 4. Spline of TM to individual parameters (a) emission, (b) temperature, (c) relative humidity. The grey background around the line are 95% confidence bounds for the response. The short lines on x axes show the distribution of data points. The number in the bracket of ordinate title is the estimated degree of freedom. The dots in the figure are the residuals.

trajectories from the south increased from 9.2% during the PRE_LOCK sub-period to 18.7% during the LOCK sub-period (Fig. S8), the TM concentrations increased by 0.21 ng/m^3 correspondingly.

3.4. Policy implications and scientific gaps

The tragic COVID-19 pandemic provided us with the chance to conduct a natural experiment to examine the effectiveness of anthropogenic control measures and to explore this gap in scientific research. The almost linear relationship between anthropogenic Hg emissions and TM concentrations indicated that emission reductions controlled TM pollution. Based on the overall synchronous decrease in both TM concentrations and Hg emissions between the same period of 2019 and 2020, we believe that Hg emission reductions still dominate the inter-annual TM variation trend in BTH currently. Existing air pollution control measures continue to aid the mitigation of atmospheric Hg pollution. As the largest emission source in China and one of the Convention-related sources, future emission reductions from CEM will benefit atmospheric TM pollution control, based on the results from the BTH region. In addition, the construction of regional joint defenses and control mechanisms should be enhanced to reduce atmospheric TM in Beijing, especially the emissions in the south of Beijing, based on the impact of the 48-h backward trajectory.

The contrasting trend between TM concentrations and Hg emissions during the LOCK sub-period of 2020 also highlights the significance of meteorology on future TM concentration trends. Unfavorable meteorology can increase the TM concentration by as much as 3.01 ng/m^3. Without the unprecedented emission reductions due to the combined effect of existing pollution control measures and COVID-19 lockdown measures, TM concentrations during the LOCK sub-period of 2020 would have exceeded those during the same period of 2019, which highlights the significance of future climate variations. According to the Convention, new sources and existing sources should take measures to control their emissions before 2022 and 2027, respectively (UNEP, 2013). Thus, global atmospheric TM concentrations are expected to decrease in the coming years with dense anthropogenic effort (Pacyna et al., 2016).

Table 1
The impact of dominant variables on TM variation.

Variables	TM variation (ng/m^3)
Anthropogenic control	−0.17
CEM	−0.11
RCC	0.02
CFPP	−0.05
ISP	−0.01
Surface meteorology	0.27
Temperature	0.09
Relative humidity	0.17
High altitude meteorology	−0.03
Boundary layer height	−0.02
Air transmission	0.17
Latitude of 48 h trajectory	0.21

However, climate change will increase global temperatures and lead to the occurrence of warm and humid weather in large parts of the world (IPCC, 2014), which is conducive to the increase of TM concentrations, according to this study. Thus, with the gradual exhaust of emission reductions from anthropogenic sources, the enhancement of natural emissions and re-emission due to climate change may lead to a returning point in TM concentrations before the appearance of a new balance in Hg between the atmosphere and surface ecosystem. To reduce Hg emissions more effectively, existing Hg pollution control measures need to cooperate with the reduction measures of carbon emissions. It is necessary to combine the Hg emission model, greenhouse gas emission model, Hg transfer model, as well as the climate change model to conduct a comprehensive evaluation. Accurate estimations of historical Hg emissions and releases are also required to evaluate current Hg loads in the air as well as the surface ecosystem and their potential re-emission.

Moreover, our study identified the importance of relative humidity on TM concentrations during the LOCK sub-period. This could be because liquid aerosol enhanced Hg photoreduction, based on a previous isotope study (Huang et al., 2019). This process is supposed to change global Hg cycling (Horowitz et al., 2017), but details on this are still unclear. A model study assumed that Hg liquid reduction occurs when relative humidity is higher than 35% and that the reaction rate is independent of relative humidity (Horowitz et al., 2017). However, the spline of relative humidity indicated a positive correlation between TM and relative humidity. This means that if the relative humidity affects the liquid reduction of Hg by changing the phase state of particles, then the assumption about the liquid phase (when relative humidity is higher than 35%) requires reconsideration. Otherwise, relative humidity may directly or indirectly impact the reaction rate. To summarize, we still need to understand the physicochemical and biogeochemical transformation of Hg in the atmosphere and at atmospheric interfaces to evaluate the effect of future climate change on Hg behavior, especially the impact from relative humidity.

Author contributions

Q.W. and S.W. designed the study. Q.W., Y.T., L.W., D.M., D.W., Y.Q., P.X., Z.G., and J.N. prepared the dataset. Q.W. conducted data analysis. Q.W., Y.T., and S.W. wrote the manuscript with contributions from all the other co-authors.

Declaration of competing interest

The authors declare that they have no known competing financial interests or personal relationships that could have appeared to influence the work reported in this paper.

Acknowledgements

This work was supported by National Key Research and Development Program of China (2017YFC0213005), National Natural Science

Foundation of China (21625701), Beijing Municipal Commission of Science and Technology (Z191100009119001 & Z191100009119004), and National Research Program for Key Issues in Air Pollution Control, China (No. DQGG0209).

We would like to thank Dian Ding for helping us extract the WRF data.

Appendix A. Supplementary data

S1. Establishment of the Emission Inventory; S2. TM Observation; S3. Model Building and Prediction. S4. Sectoral Hg Emissions in 2019; S5. Drivers of TM Variation. Supplementary data to this article can be found online at https://doi.org/10.1016/j.scitotenv.2020.142323.

References

Aldrin, M., Haff, I., 2005. Generalised additive modelling of air pollution, traffic volume and meteorology. Atmos. Environ. 39, 2145–2155.
Change IPoC (IPCC). Climate change, 2014. Synthesis Report. Contribution of Working Groups I, II and III to the Fifth Assessment Report of the Intergovernmental Panel on Climate Change. Geneva, Switzerland. vol. 2014.
Chen, L., Liang, S., Liu, M., Yi, Y., Mi, Z., Zhang, Y., et al., 2019. Trans-provincial health impacts of atmospheric mercury emissions in China. Nat. Commun. 10, 1–12.
China SCotPsRo (SC), 2013. Air Pollution and Prevention Action Plan. Beijing, China.
China SCotPsRo (SC), 2018. Three-year Action Plan for Clean Air. Beijing, China.
Fu, X.W., Zhang, H., Yu, B., Wang, X., Lin, C.J., Feng, X.B., 2015. Observations of atmospheric mercury in China: a critical review. Atmos. Chem. Phys. 15, 9455–9476.
Fushiki, T., 2009. Estimation of prediction error by using K-fold cross-validation. Stat. Comput. 21, 137–146.
Gianga, A., Selina, N.E., 2016. Benefits of mercury controls for the United States. Proc. Natl. Acad. Sci. U. S. A. 113, 286–291.
Gong, X., Kaulfus, A., Nair, U., Jaffe, D.A., 2017. Quantifying O-3 impacts in urban areas due to wildfires using a generalized additive model. Environ. Sci. Technol. 51, 13216–13223.
Gong, X., Hong, S., Jaffe, D.A., 2018. Ozone in China: spatial distribution and leading meteorological factors controlling O-3 in 16 Chinese cities. Aerosol Air Qual. Res. 18, 2287–2300.
Horowitz, H.M., Jacob, D.J., Zhang, Y.X., Dibble, T.S., Slemr, F., Amos, H.M., et al., 2017. A new mechanism for atmospheric mercury redox chemistry: implications for the global mercury budget. Atmos. Chem. Phys. 17, 6353–6371.
Hu, R., Xu, Q., Wang, S., Hua, Y., Bhattarai, N., Jiang, J., et al., 2020. Chemical characteristics and sources of water-soluble organic aerosol in southwest suburb of Beijing. J. Environ. Sci. 95, 99–110.
Huang, Q., Chen, J.B., Huang, W.L., Reinfelder, J.R., Fu, P.Q., Yuan, S.L., et al., 2019. Diel variation in mercury stable isotope ratios records photoreduction of PM2.5-bound mercury. Atmos. Chem. Phys. 19, 315–325.
Hui, M.L., Wu, Q.R., Wang, S.X., Liang, S., Zhang, L., Wang, F.Y., et al., 2017. Mercury flows in China and global drivers. Environ. Sci. Technol. 51, 222–231.
Kissinger, H.E., 1957. Reaction kinetics in differential thermal analysis. Anal. Chem. 29, 1702–1706.
Landis, M.S., Vette, A.F., Keeler, G.J., 2002. Atmospheric mercury in the Lake Michigan basin: influence of the Chicago/Gary urban area. Environ. Sci. Technol. 36, 4508–4517.
Liu, K.Y., Wang, S.X., Wu, Q.R., Wang, L., Ma, Q., Zhang, L., et al., 2018. A highly resolved mercury emission inventory of Chinese coal-fired power plants. Environ. Sci. Technol. 52, 2400–2408.
Liu, J.J., Wang, L., Zhu, Y., Lin, C.J., Jang, C., Wang, S.X., et al., 2019a. Source attribution for mercury deposition with an updated atmospheric mercury emission inventory in the Pearl River Delta Region, China. Front. Environ. Sci. Eng. 14, 1–11.
Liu, K.Y., Wu, Q.R., Wang, L., Wang, S.X., Liu, T.H., Ding, D., et al., 2019b. Measure-specific effectiveness of air pollution control on China's atmospheric mercury concentration and deposition during 2013-2017. Environ. Sci. Technol. 53, 8938–8946.
Pacyna, J.M., Travnikov, O., De Simone, F., Hedgecock, I.M., Sundseth, K., Pacyna, E.G., et al., 2016. Current and future levels of mercury atmospheric pollution on a global scale. Atmos. Chem. Phys. 16, 12495–12511.
Pannu, R., Siciliano, S.D., O'Driscoll, N.J., 2014. Quantifying the effects of soil temperature, moisture and sterilization on elemental mercury formation in boreal soils. Environ. Pollut. 193, 138–146.
Polissar, A.V., Hopke, P.K., Paatero, P., Kaufmann, Y.J., Hall, D.K., Bodhaine, B.A., et al., 1999. The aerosol at Barrow, Alaska: long-term trends and source locations. Atmos. Environ. 33, 2441–2458.
Qin, X.F., Wang, X.H., Shi, Y.J., Yu, G.Y., Zhao, N., Lin, Y.F., et al., 2019. Characteristics of atmospheric mercury in a suburban area of East China: sources, formation mechanisms, and regional transport. Atmos. Chem. Phys. 19, 5923–5940.
Saiz-Lopez, A., Sitkiewicz, S.P., Roca-Sanjuan, D., Oliva-Enrich, J.M., Davalos, J.Z., Notario, R., et al., 2018. Photoreduction of gaseous oxidized mercury changes global atmospheric mercury speciation, transport and deposition. Nat. Commun. 9.
Skamarock, W.C., Klemp, J.B., Dudhia, J., Gill, D.O., Barker, D.M., Duda, M.G., et al., 2008. A Description of the Advanced Research WRF Version 3 (No. NCAR/TN-475+STR).
Sprovieri, F., Pirrone, N., Bencardino, M., D'Amore, F., Carbone, F., Cinnirella, S., et al., 2016. Atmospheric mercury concentrations observed at ground-based monitoring sites globally distributed in the framework of the GMOS network. Atmos. Chem. Phys. 16, 11915–11935.
Tang, Y., Wang, S.X., Wu, Q.R., Liu, K.Y., Wang, L., Li, S., et al., 2018. Recent decrease trend of atmospheric mercury concentrations in East China: the influence of anthropogenic emissions. Atmos. Chem. Phys. 18, 8279–8291.
Tang, Y., Wang, S.X., Wu, Q.R., Liu, K.Y., Li, Z.J., Zou, J., et al., 2019. Measurement of size-fractionated particulate-bound mercury in Beijing and implications on sources and dry deposition of mercury. Sci. Total Environ. 675, 176–183.
Tian, H.Z., Zhu, C.Y., Gao, J.J., Cheng, K., Hao, J.M., Wang, K., et al., 2015. Quantitative assessment of atmospheric emissions of toxic heavy metals from anthropogenic sources in China: historical trend, spatial distribution, uncertainties, and control policies. Atmos. Chem. Phys. 15, 10127–10147.
United Nations Environment Programme (UNEP), 2013. Minamata Convention on Mercury. UNEP, Minamata, Japan.
Wang, X., Lin, C.J., Yuan, W., Sommar, J., Zhu, W., Feng, X.B., 2016. Emission-dominated gas exchange of elemental mercury vapor over natural surfaces in China. Atmos. Chem. Phys. 16, 11125–11143.
Wen, M., Wu, Q., Li, G., Wang, S., Li, Z., Tang, Y., et al., 2020. Impact of ultra-low emission technology retrofit on the mercury emissions and cross-media transfer in coal-fired power plants. J. Hazard. Mater. 396 (1–8).
Wood, S.N., 2013. On p-values for smooth components of an extended generalized additive model. Biometrika 100, 221–228.
Wu, Q.R., Wang, S.X., Li, G.L., Liang, S., Lin, C.-J., Wang, Y.F., et al., 2016. Temporal trend and spatial distribution of speciated atmospheric mercury emissions in China during 1978–2014. Environ. Sci. Technol. 50, 13428–13435.
Wu, Q.R., Gao, W., Wang, S.X., Hao, J.M., 2017. Updated atmospheric speciated mercury emissions from iron and steel production in China during 2000-2015. Atmos. Chem. Phys. 17, 10423–10433.
Wu, Q., Li, G., Wang, S., Liu, K., Hao, J., 2018a. Mitigation options of atmospheric Hg emissions in China. Environ. Sci. Technol. 52, 12368–12375.
Wu, Q.R., Wang, S.X., Liu, K.Y., Li, G.L., Hao, J.M., 2018b. Emission-limit-oriented strategy to control atmospheric mercury emissions in coal-fired power plants towards the implementation of Minamata Convention. Environ. Sci. Technol. 52, 11087–11093.
Yin, X.F., Kang, S.C., de Foy, B., Ma, Y.M., Tong, Y.D., Zhang, W., et al., 2018. Multi-year monitoring of atmospheric total gaseous mercury at a remote high-altitude site (Nam Co, 4730 m a.s.l.) in the inland Tibetan Plateau region. Atmos. Chem. Phys. 18, 10557–10574.
Zhang, L., Wang, S.X., Wang, L., Wu, Y., Duan, L., Wu, Q.R., et al., 2015. Updated emission inventories for speciated atmospheric mercury from anthropogenic sources in China. Environ. Sci. Technol. 49, 3185–3194.